Taylor & Francis
Taylor & Francis Group

Combustion Theory and Modelling

ISSN: 1364-7830 (Print) 1741-3559 (Online) Journal homepage: https://www.tandfonline.com/loi/tctm20

Initiation and propagation of spherical premixed flames with inert solid particles

Qiang Li, Chaoyi Liu, Huangwei Zhang, Mengze Wang & Zheng Chen

To cite this article: Qiang Li, Chaoyi Liu, Huangwei Zhang, Mengze Wang & Zheng Chen (2020): Initiation and propagation of spherical premixed flames with inert solid particles, Combustion Theory and Modelling, DOI: 10.1080/13647830.2020.1725135

To link to this article: https://doi.org/10.1080/13647830.2020.1725135

Combustion Theory and Modelling, 2020
https://doi.org/10.1080/13647830.2020.1725135

Initiation and propagation of spherical premixed flames with inert solid particles

Qiang Li[a], Chaoyi Liu[b], Huangwei Zhang [a*], Mengze Wang[b] and Zheng Chen [b]

[a]*Department of Mechanical Engineering, Faculty of Engineering, National University of Singapore, Singapore 117575, Singapore;* [b]*SKLTCS, CAPT, BIC-ESAT, College of Engineering, Peking University, Beijing 100871, People's Republic of China*

(*Received 17 April 2019; accepted 17 January 2020*)

Spherical flame initiation and propagation in particle-laden mixtures are investigated theoretically in this work. Within the framework of constant density, large activation energy and quasi-steady assumptions, a correlation describing spherical flame propagation speed as a function of flame radius is derived. This correlation is used to assess the influence of gas and particle properties on initiation and propagation of premixed spherical flames. Spherical flame initiation and propagation are shown to be influenced noticeably by the appearance of inert solid particles. It is found that the flame propagation speed and temperature both decrease with increased particle heat capacity and thermal relaxation time. A non-monotonic change of the flame propagation speed with flame radius is observed when there are particles with large heat capacity. Furthermore, the bifurcation of flame propagation speed is observed for particles with large heat capacity and thermal relaxation time. Within a certain flame radius range, there are both strong and weak flame solutions. The abrupt jump from the strong flame to weak flame results from the excessive heat loss caused by the solid particles and the energy balance is re-established along the weak flame branch. The Lewis number strongly affects the flame propagation speed, particularly for small thermal response time and high particle heat capacity. Additionally, the minimum ignition energy of the particle-laden spherical flames is found to increase with the Lewis number. At higher Lewis number, the difference of minimum ignition energy between gaseous and particle-laden situations becomes larger. To validate the theoretical results, one-dimensional transient simulations of particle-laden spherical flames with detailed chemistry have been conducted. Qualitative agreement is achieved for results from numerical simulations and theoretical analysis.

Keywords: Inert solid particle; spherical flame; ignition; flame propagation; Lewis number

1. Introduction

Gaseous combustion laden with dispersed solid particles is quite common in practical engineering applications, e.g. pulverised coal combustion, sooty flames in gas turbine engines and even in novel material synthesis. Some of these particles are burned as fuels, while others are generated intrinsically from the combustion processes. The existence of solid particles may result in new phenomena in the combustion process, due to the inter-phase interactions in terms of mass, momentum and energy exchanges [1].

*Corresponding author. Email: huangwei.zhang@nus.edu.sg; mpezhu@nus.edu.sg

For the premixed flames laden with inert solid particles, Joulin [2] and Mitani [3] theoretically studied the effects of heat conduction between gas and particles. They found that the presence of solid particles leads to a considerable decrease in flame speed. When the particle size exceeds a critical value, the variation of flame speed with particle concentration was not monotonic and multiplicity of the flame speed appears. However, in the experiments of Mitani and Niioka [4], the flame speed was observed to monotonically decrease with particle concentration. Blouquin et al. [5,6] studied the radiation-induced dynamics of particle-laden spherical flames. Ju and Law [7] found that heat transfer caused by the particles has a strong impact on flame temperature, flame propagation speed and flammability limit, and it also results in various flame regimes. The inter-phase momentum exchange between gas and particle phases and its effects on flame propagation and extinction in various gravity conditions were discussed by Makhviladze et al. [8]. They observed that the propagating flame can extinguish abruptly when the particle loading is sufficiently large. In spite of the above previous investigations, there are still limited studies on how the solid particles affect initiation and propagation of premixed spherical flames with positive stretch.

The propagating spherical flame has been widely used in theoretical studies because of its simple geometry. For instance, the effects of thermal expansion and Lewis number were discussed by Frankel and Sivashinsky [9]. Chung and Law [10] performed integral analysis for the propagating spherical flames, while Ronney and Sivashisky [11] studied the outwardly propagating spherical flame using slowly varying flame theory. Bechtold et al. [12–14] investigated the hydrodynamic and thermal-diffusion instabilities and the radiation heat loss in propagating spherical flames. He [15] studied the critical conditions for spherical flame initiation in a mixture with large Lewis number and found that the conditions for the existence of a self-sustained propagating spherical flame determine the critical power and energy of the ignition source for successful initiation. Chen and Ju [16] found that the spherical flame initiation was considerably influenced by fuel Lewis number and radiation heat loss. Recently, the role of thermally sensitive intermediate kinetics in initiation and propagation of spherical flames was discussed through considering the two-step chemistry [17–19]. It was found that the transport and reaction of radicals have quantitative rather than qualitative effects on ignition and spherical flame propagation.

For two-phase spherical flames, Greenberg [20] derived an evolution equation for a laminar spherical flame front propagating into a spray mist cloud. Han and Chen [21] assessed the effects of finite rate vapourisation on ignition and propagation of spherical spray flames. Zhuang and Zhang theoretically investigated the water-droplet-laden premixed spherical flames for fully and partially droplet distributions, and it is found that the presence of the water droplets has significant influence on the flame initiation, propagation and extinction [22]. For spherical flames with inert solid particles, Blouquin et al. [5,6] analytically studied the radiation heat loss effects, but the effect on flame extinction was not mentioned. Qiao [23] has conducted a one-dimensional simulation to study the transient flame propagation process and flame speed oscillation phenomenon in a carbon dust cloud. However, to the authors' best knowledge, no theoretical analysis was performed to understand the influence of inter-phase coupling on spherical flame initiation and propagation.

The objective of this work is to examine the effects of chemically inert solid particles on spherical flame initiation and propagation through theoretical analysis. The focus is on the effects of Lewis number and solid particle properties on flame propagation, flame regime and Minimum Ignition Energy (MIE) for the particle-laden premixed spherical flames. The rest of the paper is structured as below. The mathematical models for the particle phase and

gas phase are presented in Section 2, and the analytical solutions are shown in Section 3. In Section 4, the effects of solid particle properties and gaseous species Lewis number are assessed. The theoretical analysis is validated through the transient simulations in Section 5. Finally, the conclusions are made in Section 6.

2. Mathematical model

In this work, one-dimensional particle-laden spherical premixed flame is considered. We assume that the thermal properties and transport coefficients are constant [7,15,16–19,24–27,28], such as density and thermal conductivity. Chemically inert solid particles are uniformly dispersed in the gaseous pre-mixture. The Eulerian description is adopted for the particle phase, which is treated as an inter-penetrating continuum [1]. Due to the dilute particle concentration, the inter-particle collisions are not considered and therefore the diffusion terms in the equations for particle phase are neglected. The inter-phase kinetic equilibrium is assumed, and their velocity difference is neglected. The particles are spherical and their properties (e.g. diameter, density and heat capacity) are assumed to be constant. The above assumptions for the particle phase are also used in previous theoretical work on particle-laden flames [5–7]. Radiative heat transfer is not considered in this work. Although it may be critical for particle-laden flame dynamics as shown in Refs. [5–7], here we mainly focus on the effects of convective heat transfer on spherical flames and the radiation effects will be investigated in a future study. The validity of the above assumptions will be further examined in Section 5 through transient numerical simulations considering detailed chemistry and particle models.

Under the above assumptions, the equation for the gas phase temperature is

$$\tilde{\rho}_g \tilde{C}_{p,g} \frac{\partial \tilde{T}_g}{\partial \tilde{t}} = \frac{1}{\tilde{r}^2} \frac{\partial}{\partial \tilde{r}} \left(\tilde{r}^2 \tilde{\lambda} \frac{\partial \tilde{T}_g}{\partial \tilde{r}} \right) + \tilde{q}_r \tilde{\omega}_r - \tilde{n}_p \tilde{q}_c, \tag{1}$$

where $\tilde{\rho}_g$ is the density, $\tilde{C}_{p,g}$ is the gas specific heat capacity at constant pressure, $\tilde{\lambda}$ is the thermal conductivity, $\tilde{q}_r$ is the heat release rate per unit mass of fuel, $\tilde{n}_p$ is the particle number density, $\tilde{\omega}_r$ is the homogeneous reaction rate, and $\tilde{q}_c$ is the heat transfer between gas and particle.

Since the heat conductivity in the particle phase is much faster than that in the gas phase, the particle is assumed to have a uniform temperature. The equation for the particle phase temperature is

$$\tilde{V}_p \tilde{\rho}_p \tilde{C}_{p,p} \frac{\partial \tilde{T}_p}{\partial \tilde{t}} = \tilde{q}_c, \tag{2}$$

where $\tilde{V}_p$, $\tilde{\rho}_p$, $\tilde{C}_{p,p}$ are the particle volume, density, and specific heat capacity at constant pressure, respectively.

The heat exchange term, $\tilde{q}_c$, in Equations (1) and (2) can be estimated through

$$\tilde{q}_c = \tilde{h} \tilde{A}_p (\tilde{T}_g - \tilde{T}_p), \tag{3}$$

where $\tilde{A}_p$ is the surface area of a single particle, i.e. $\tilde{A}_p = \pi \tilde{d}_p^2$. $\tilde{d}_p$ is the particle diameter and $\tilde{h}$ is the heat transfer coefficient, which is estimated using the following correlation

from Ranz and Marshall [29]:

$$Nu = \frac{\tilde{h}\tilde{d}_p}{\tilde{\lambda}} = 2.0 + 0.6\,\mathrm{Re}^{1/2}Pr^{1/3} \tag{4}$$

where Nu, Pr and Re are the Nusselt number, Prandtl number and particle Reynolds number, respectively. We can neglect the effect of particle Reynolds number Re due to the assumption of kinetic equilibrium and therefore $Nu \approx 2$. Therefore, Equation (3) becomes

$$\tilde{q}_c = 2\pi\tilde{d}_p\tilde{\lambda}(\tilde{T}_g - \tilde{T}_p). \tag{5}$$

For gas phase chemistry, one-step, irreversible, Arrhenius type reaction ($F + O \rightarrow P$) is adopted. The mass fraction equation under fuel-lean condition is for fuel F, while under fuel-rich condition it is for oxidiser O. The respective equations for these two cases are

$$\tilde{\rho}_g\frac{\partial\tilde{Y}_F}{\partial\tilde{t}} = \frac{1}{\tilde{r}^2}\frac{\partial}{\partial\tilde{r}}\left(\tilde{r}^2\tilde{\rho}_g\tilde{D}_F\frac{\partial\tilde{Y}_F}{\partial\tilde{r}}\right) - \tilde{\omega}_r, \tag{6}$$

$$\tilde{\rho}_g\frac{\partial\tilde{Y}_O}{\partial\tilde{t}} = \frac{1}{\tilde{r}^2}\frac{\partial}{\partial\tilde{r}}\left(\tilde{r}^2\tilde{\rho}_g\tilde{D}_O\frac{\partial\tilde{Y}_O}{\partial\tilde{r}}\right) - \tilde{\omega}_r, \tag{7}$$

where $\tilde{Y}_F$ and $\tilde{Y}_O$ are mass fractions of fuel and oxidiser, respectively. $\tilde{D}_F$ and $\tilde{D}_O$ are mass diffusivities of fuel and oxidiser, respectively.

The reaction rate $\tilde{\omega}_r$ in Equation (1) is

$$\tilde{\omega}_r = \tilde{\rho}_g\tilde{A}\tilde{Y}_F^{\alpha}\tilde{Y}_O^{1-\alpha}\exp(-\tilde{E}/\tilde{R}^0\tilde{T}_g), \tag{8}$$

where α is 1 for fuel-lean case and 0 for fuel-rich case. The quantities $\tilde{A}$, $\tilde{E}$, $\tilde{R}^0$ in Equation (8) are the pre-factor of Arrhenius law, activation energy and the universal gas constant, respectively.

The boundary conditions at the spherical centre ($\tilde{r} = 0$) and unburned far-field ($\tilde{r} \rightarrow \infty$) are specified as below

$$\tilde{r} = 0:\ \tilde{r}^2\frac{\partial\tilde{T}_g}{\partial\tilde{r}} = -\frac{\tilde{Q}}{4\pi\tilde{\lambda}},\ \partial\tilde{Y}_F/\partial\tilde{r} = 0,\ \partial\tilde{Y}_O/\partial\tilde{r} = 0, \tag{9}$$

$$\tilde{r} \rightarrow \infty:\ \tilde{T}_g = \tilde{T}_u,\ \tilde{T}_p = \tilde{T}_u,\ \tilde{Y}_F = \tilde{Y}_{F,u},\ \tilde{Y}_O = \tilde{Y}_{O,u}, \tag{10}$$

in which the subscript u denotes the unburned fresh mixture, and $\tilde{Q}$ denotes the energy from the central ignition source, to mimic the external energy deposition at the spherical centre. This ignition model is similar to the one used in the previous theoretical analysis [15–17,30] and is adequate to obtain qualitative understanding of spherical flame initiation and propagation, based on the numerical results in Refs. [16,17].

To improve the universality of theoretical analysis, the above equations and boundary conditions can be normalised. The reference variables are introduced, including the adiabatic planar gaseous flame speed $\tilde{u}_{ad}$, the adiabatic planar gaseous flame temperature $\tilde{T}_{ad}$, the flame thickness $\tilde{l}_{ad}$ and other relevant quantities at the unburned zone (i.e. $\tilde{T}_u$, $\tilde{Y}_{F,u}$ and $\tilde{Y}_{O,u}$).

For the reference variables $\tilde{u}_{ad}$, $\tilde{T}_{ad}$ and $\tilde{l}_{ad}$, they can be expressed as [25]

$$\tilde{u}_{ad} = \left[\frac{2\tilde{\lambda}Le_F^{\alpha}Le_O^{1-\alpha}}{\tilde{\rho}_g\tilde{C}_{p,g}Z^2}\tilde{A}\exp\left(-\frac{\tilde{E}}{\tilde{R}^0\tilde{T}_{ad}}\right)\right]^{\frac{1}{2}}, \tilde{T}_{ad} = \tilde{T}_u + \frac{\tilde{q}_r\tilde{Y}_{F,u}^{\alpha}\tilde{Y}_{O,u}^{1-\alpha}}{\tilde{C}_{p,g}}, \tilde{l}_{ad} = \frac{\tilde{\lambda}}{\tilde{\rho}_g\tilde{C}_{p,g}\tilde{u}_{ad}}, \tag{11}$$

where $Z = \tilde{E}(\tilde{T}_{ad} - \tilde{T}_u)/\tilde{R}^0\tilde{T}_{ad}^2$ is the Zel'dovich number. *Le* is the Lewis number of the deficient species (fuel or oxidiser).

With the above reference variables, the following normalisation can be made

$$r = \frac{\tilde{r}}{\tilde{l}_{ad}}, t = \frac{\tilde{t}}{\tilde{l}_{ad}/\tilde{u}_{ad}}, T_g = \frac{\tilde{T}_g - \tilde{T}_u}{\tilde{T}_{ad} - \tilde{T}_u}, T_p = \frac{\tilde{T}_p - \tilde{T}_u}{\tilde{T}_{ad} - \tilde{T}_u}, Y_F = \frac{\tilde{Y}_F}{\tilde{Y}_{F,u}}, Y_O = \frac{\tilde{Y}_O}{\tilde{Y}_{O,u}}, u = \frac{\tilde{u}}{\tilde{u}_{ad}}. \tag{12}$$

Substituting Equation (12) into Equations (1), (2), (6) and (7) yields the following dimensionless equations for gas and particle phases

$$\frac{\partial T_g}{\partial t} = \frac{1}{r^2}\frac{\partial}{\partial r}\left(r^2\frac{\partial T_g}{\partial r}\right) + \omega_r - \frac{CK(T_g - T_p)}{Z}, \tag{13}$$

$$\frac{\partial Y_F}{\partial t} = \frac{Le_F^{-1}}{r^2}\frac{\partial}{\partial r}\left[r^2\frac{\partial Y_F}{\partial r}\right] - \omega_r, \tag{14}$$

$$\frac{\partial Y_O}{\partial t} = \frac{Le_O^{-1}}{r^2}\frac{\partial}{\partial r}\left[r^2\frac{\partial Y_O}{\partial r}\right] - \omega_r, \tag{15}$$

$$\frac{\partial T_p}{\partial t} = K(T_g - T_p), \tag{16}$$

where the non-dimensional quantities present in Equations (13)–(16) are

$$\omega_r = \frac{1}{2Le_F^{\alpha}Le_O^{1-\alpha}}Y_F^{\alpha}Y_O^{1-\alpha}Z^2\exp\left(\frac{Z(T_g - 1)}{\sigma + (1-\sigma)T_g}\right), \tag{17}$$

$$\sigma = \frac{\tilde{\rho}_{ad}}{\tilde{\rho}_u} = \frac{\tilde{T}_u}{\tilde{T}_{ad}}, \tag{18}$$

$$K = \frac{\tilde{\lambda}^2/(\tilde{\rho}_g\tilde{C}_{p,g}\tilde{u}_{ad}^2)}{\tilde{C}_{p,p}\tilde{\rho}_p\tilde{d}_p^2/12} = \frac{\tilde{\lambda}}{(1/6)\tilde{d}_p^2\tilde{\rho}_p\tilde{C}_{p,p}Le_F^{\alpha}Le_O^{1-\alpha}\tilde{A}}Z^2\exp(\frac{\tilde{E}}{\tilde{R}^0\tilde{T}_{ad}}), \tag{19}$$

$$C = Z\frac{\tilde{n}_p\tilde{\rho}_p\tilde{C}_{p,p}\pi\tilde{d}_p^3/6}{\tilde{\rho}_g\tilde{C}_{p,g}}, \tag{20}$$

where ω_r is the non-dimensional reaction rate, σ is thermal expansion ratio, K (termed as 'particle thermal relaxation time' hereafter) is the ratio of the residence time in the preheat zone to the thermal relaxation time of the particles, while C (termed as 'particle heat capacity' hereafter) is the ratio of heat capacity of particles to the heat capacity of gas mixture [7]. For parameter K, it essentially denotes the response time of the solid particle to reach thermal equilibrium with the local gas mixture. The lower K, the longer thermal response time, and therefore the lower heat exchange rate and slower change rate of gas

temperature. For the parameter C, it quantifies the relative magnitudes of heat capacities of the particle and gas phases. Noticeably, C is also a function of particle number density $\tilde{n}_p$. Specifically, the lower C, the smaller the reduction of gas temperature for a fixed amount of heat transferred from the gas to particles, and accordingly the less obvious the effects of solid particles on the gas phase. Note that the particle temperature is only affected by K, whilst the gas phase temperature is affected by both C and K. Their influences on flame initiation and propagation will be discussed in detail in Section 4.

The typical values for the above particle properties, i.e. C and K in Equations (19) and (20), can be estimated, assuming that they are dispersed in a hydrogen/air combustion system. The particle diameter and number density of interest range from 10 to 100 μm and 1000–10,000 cm^{-3}, respectively. The material density of the solid particle is assumed to be 1,500kg/m^3, while the specific heat capacity is 500 J/(kg·K). For stoichiometric H_2/air flames, the laminar flame speed $\tilde{u}_{ad}$ is about 2.15 m/s, the density of the pre-mixture $\tilde{\rho}_g$ is around 0.24 kg/m^3, the heat capacity $\tilde{C}_{p,g}$ is about 5000 J/(kg K), and the heat conductivity $\tilde{\lambda}$ is 0.18 W/(m K). These parameters are extracted from our transient numerical simulations in Section 5. The relevant ranges of C and K corresponding to variable particle diameters and number densities are 0.003-70 and 0.01-1, respectively.

The dimensionless boundary conditions, corresponding to Equations (9) and (10), are

$$r = 0: \ \frac{r^2 dT_g}{\partial r} = -Q, \ \frac{dY_F}{\partial r} = \frac{dY_O}{\partial r} = 0, \tag{21}$$

$$r \to \infty: \ T_g = T_p = 0, \ Y_F = 1, Y_O = 1. \tag{22}$$

The dimensionless ignition energy Q in Equation (21) is

$$Q = \frac{\tilde{Q}}{4\pi \tilde{l}_{ad} \tilde{\lambda} (\tilde{T}_{ad} - \tilde{T}_u)}. \tag{23}$$

To further simplify the theoretical analysis, we study the propagating spherical flame in the coordinate attached to the moving flame front $r = R(t)$ (dimensionless form). Accordingly, the spatial coordinate is transformed into $\eta = r - R(t)$. Meanwhile, since the critical flame radius for propagating spherical flames is larger than the flame thickness, the time scale based on the critical flame radius is larger than the flame transient time. Therefore, the propagation of the flame front can be considered as in a quasi-steady state in η coordinate system [15]. The steady-state assumption has been successfully used in the theoretical analysis of premixed flames in both purely gaseous [9,15–19,24,25] and two-phase [7,21,22] pre-mixture. In addition, its validity has been confirmed from the previous studies through transient numerical simulations [15–18]. With the above assumptions, the equations for the gas phase and particle phase can be rewritten in η coordinate system as

$$-U\frac{dT_g}{d\eta} = \frac{1}{(\eta + R)^2}\frac{d}{d\eta}\left[(\eta + R)^2 \frac{dT_g}{d\eta}\right] + \omega_r - \frac{CK(T_g - T_p)}{Z}, \tag{24}$$

$$-U\frac{dY_F}{d\eta} = \frac{Le_F^{-1}}{(\eta + R)^2}\frac{d}{d\eta}\left[(\eta + R)^2 \frac{dY_F}{d\eta}\right] - \omega_r, \tag{25}$$

$$-U\frac{dY_O}{d\eta} = \frac{Le_O^{-1}}{(\eta + R)^2}\frac{d}{d\eta}\left[(\eta + R)^2 \frac{dY_O}{d\eta}\right] - \omega_r, \tag{26}$$

$$-U\frac{dT_p}{d\eta} = K(T_g - T_p), \tag{27}$$

in which $U = dR(t)/dt$ is the flame propagating speed and the non-dimensional boundary conditions in the new coordinate $\eta = r - R(t)$ read

$$\eta = -R : (\eta + R)^2\frac{dT_g}{d\eta} = -Q, \frac{dY_F}{d\eta} = \frac{dY_O}{d\eta} = 0, \tag{28}$$

$$\eta \to \infty : \ T_g = T_p = 0, Y_F = 1, \ Y_o = 1. \tag{29}$$

3. Theoretical analysis

3.1. *Analytical solution*

The large activation energy assumption is applied in this study. With this, chemical reactions are assumed to be confined at an infinitesimally thin flame sheet ($\eta = 0$). This simplification is used for theoretical analysis of both gaseous [15–19] and particle- or droplet-laden [5–7,20–22] flames, and is shown to be adequate to predict the main characteristics of flame dynamics, such as ignition and propagation. Therefore, the governing equations for gas and particle phases in the burned zone ($\eta < 0$) and unburned ($\eta > 0$) zone read

$$-U\frac{dT_g}{d\eta} = \frac{1}{(\eta + R)^2}\frac{d}{d\eta}\left[(\eta + R)^2\frac{dT_g}{d\eta}\right] - \frac{CK(T_g - T_p)}{Z}, \tag{30}$$

$$-U\frac{dY_F}{d\eta} = \frac{Le_F^{-1}}{(\eta + R)^2}\frac{d}{d\eta}\left[(\eta + R)^2\frac{dY_F}{d\eta}\right], \tag{31}$$

$$-U\frac{dY_O}{d\eta} = \frac{Le_O^{-1}}{(\eta + R)^2}\frac{d}{d\eta}\left[(\eta + R)^2\frac{dY_O}{d\eta}\right], \tag{32}$$

$$-U\frac{dT_p}{d\eta} = K(T_g - T_p). \tag{33}$$

At the flame front ($\eta = 0$), the following jump conditions hold [25]

$$T_g = T_f, \ [T_p] = 0, \ Y_F^{\alpha}Y_O^{1-\alpha} = 0, \tag{34}$$

$$\begin{aligned}\frac{dT_g}{d\eta}|_{0^+} - \frac{dT_g}{d\eta}|_{0^-} &= \frac{1}{Le_F^{\alpha}Le_O^{1-\alpha}}\left(\frac{d(Y_F^{\alpha}Y_O^{1-\alpha})}{d\eta}|_{0^+} - \frac{d(Y_F^{\alpha}Y_O^{1-\alpha})}{d\eta}|_{0^-}\right)\\ &= [\sigma + (1-\sigma)T_f]^2\exp\left[\frac{Z}{2}\frac{T_f - 1}{\sigma + (1-\sigma)T_f}\right].\end{aligned} \tag{35}$$

The subscript '0^+' denotes the quantities at the unburned size of the flame front, while '0^-' denotes the quantities at the burned side. One can obtain the exact solutions through analytically solving Equations (30)–(33) with the boundary conditions, i.e. Equations (28) and (29), and jump conditions, i.e. Equations (34) and (35), and their exact solutions will be given below.

The analytical expressions of particle temperature T_p read

$$T_p(\eta) = \begin{cases} C_1 I_1(\eta) - (C_1 - C_2)\left[\dfrac{I_1'(0)}{I_2'(0)} I_2(\eta) + I_1(0)\right] & -R < \eta < 0. \\ -\dfrac{T_f}{\frac{U}{K} I_1'(0) - I_1(0)} I_1(\eta) & 0 < \eta < \infty. \end{cases} \tag{36}$$

Substituting Equation (36) into Equation (27), we can obtain the solutions of gas temperature T_g as

$$T_g(\eta) = \begin{cases} C_1\left[I_1(\eta) - \dfrac{U}{K} I_1'(\eta)\right] \\ \quad -(C_1 - C_2)\left[\dfrac{I_1'(0)}{I_2'(0)}\left(I_2(\eta) - \frac{U}{K} I_2'(\eta)\right) + I_1(0)\right] & -R < \eta < 0. \\ -\dfrac{T_f}{\frac{U}{K} I_1'(0) - I_1(0)} I_1(\eta) + \frac{T_f}{I_1'(0) - \frac{K}{U} I_1(0)} I_1'(\eta) & 0 < \eta < \infty, \end{cases} \tag{37}$$

where C_1 and C_2 are the constants with the following expressions

$$C_1 = \frac{KQ(K+U^2)\Gamma\left(\frac{\sqrt{Z}(K+U^2)}{\sqrt{4CKU^2 + Z(K+U^2)^2}}\right)}{U\sqrt{\frac{4CKU^2}{Z} + (K+U^2)^2}}, \tag{38}$$

$$C_2 = \frac{KT_f}{KI_1(0) - UI_1{}'(0)}. \tag{39}$$

In Equations (36) and (37), $I_1(\eta)$ and $I_2(\eta)$ take the following form

$$I_1(\eta) = \int_\eta^\infty \left\{ \frac{1}{s+R} \exp\left[-\frac{(s+R)\left(\sqrt{4CKU^2 + Z(K+U^2)^2} + \sqrt{Z}(U^2 - K)\right)}{2U\sqrt{Z}} \right] \right.$$
$$\left. \times\ F_2\left(\frac{\sqrt{Z}(K+U^2)}{\sqrt{4CKU^2 + Z(K+U^2)^2}}, 0, \frac{(R+s)\sqrt{4CKU^2 + Z(K+U^2)^2}}{U\sqrt{Z}} \right) \right\} \mathrm{d}s, \tag{40}$$

$$I_2(\eta) = \int_0^\eta \left\{ \frac{1}{s+R} \exp\left[-\frac{(s+R)\left(\sqrt{4CKU^2 + Z(K+U^2)^2} + \sqrt{Z}(U^2 - K)\right)}{2U\sqrt{Z}} \right] \right.$$
$$\left. \times\ G\left(-\frac{\sqrt{Z}(K+U^2)}{\sqrt{4CKU^2 + Z(K+U^2)^2}}, -1, \frac{(R+s)\sqrt{4CKU^2 + Z(K+U^2)^2}}{U\sqrt{Z}} \right) \right\} \mathrm{d}s, \tag{41}$$

where

$$F_2(a,b,c) = \frac{1}{\Gamma(a)}\int_0^\infty e^{-ct}t^{a-1}(1+t)^{b-a-1}\mathrm{d}t, \tag{42}$$

$$G(a,b,c) = \frac{\Gamma(a+b+1)}{\Gamma(a+1)}F_1(-a,b+1,c), \tag{43}$$

$$F_1(a,b,c) = \frac{\Gamma(b)}{\Gamma(b-a)\Gamma(a)}\int_0^1 e^{ct}t^{a-1}(1-t)^{b-a-1}\mathrm{d}t, \quad \Gamma(z) = \int_0^\infty \frac{t^{z-1}}{e^t}\mathrm{d}t. \tag{44}$$

In Equations (42) and (43), $F_1(a, b, c)$ is the confluent Hypergeometric function of the first kind, $F_2(a, b, c)$ is the confluent Hypergeometric function of the second kind and $G(a, b, c)$ is the generalised Laguerre function [31]. In addition, in Equations (36) and (37), $I_1{}'(\eta)$ and $I_2{}'(\eta)$ are the first derivatives of $I_1(\eta)$ and $I_2(\eta)$, respectively.

The distributions of fuel (fuel-lean condition) or oxidiser (fuel-rich condition) mass fraction in burned ($-R < \eta < 0$) and unburned ($0 < \eta < \infty$) zones are

$$Y_{\{F,O\}}(\eta) = \begin{cases} 0 & -R < \eta < 0, \\ 1 - \dfrac{\int_{\eta+R}^\infty \xi^{-2}\exp(-ULe_{\{F,O\}}\xi)\mathrm{d}\xi}{\int_R^\infty \xi^{-2}\exp(-ULe_{\{F,O\}}\xi)\mathrm{d}\xi} & 0 < \eta < \infty. \end{cases} \tag{45}$$

Here the subscripts in the brackets, 'F' and 'O', for both Y and Le denote fuel and oxidiser, respectively.

The correlation between flame propagation speed U, spherical flame radius R, and flame temperature T_f can be derived based on the jump condition, Equation (35), which reads ($I_1''(\eta)$ and $I_2''(\eta)$ are the second derivatives of $I_1(\eta)$ and $I_2(\eta)$, respectively)

$$\begin{aligned} &C_1\left[I_1'(0) - \frac{U}{K}I_1''(0)\right] - (C_1 - C_2)\left[\frac{I_1'(0)}{I_2'(0)}\left(I_2'(0) - \frac{U}{K}I_2''(0)\right)\right] \\ &- \frac{T_f}{I_1(0) - \frac{U}{K}I_1'(0)}\left(-\frac{U}{K}I_1''(0) + I_1'(0)\right) \\ &= [\sigma + (1-\sigma)T_f]^2 \\ &= \frac{1}{Le_{\{F,O\}}}\frac{R^{-2}\exp(-ULe_{\{F,O\}}R)}{\int_R^\infty s^{-2}\exp(-ULe_{\{F,O\}}s)ds}\exp\left[\frac{Z}{2}\frac{T_f - 1}{\sigma + (1-\sigma)T_f}\right]. \end{aligned} \tag{46}$$

Therefore, the general theory describing initiation and propagation of spherical flames in a premixed gas mixture with inert solid particles has been derived. The effects of the Lewis number of fuel or oxidiser (Le), particle heat capacity (C), particle thermal relaxation time (K) and central ignition power (Q) can be investigated. Through numerically solving Equation (46), the relation between flame propagation speed U, flame radius R and flame temperature T_f at different flame regimes can be analysed, considering the different foregoing parameters. Note that with this correlation, both fuel-rich and fuel-lean situations can be studied. However, it can be seen that their equations literally take the identical form. As a result, the Lewis numbers of the fuel and oxidiser, Le_F and Le_O, will be not discussed separately in the following; instead, only Le is used for brevity. The current theoretical analysis can recover the results for particle-free spherical flames when the limit of $CK \to 0$ is taken in Equation (30), which corresponds to that from Refs. [16,28]. For Zel'dovich number and thermal expansion ratio in Equation (46), they are set to be $Z = 10$ and $\sigma = 0.15$, following the values used in our previous theoretical analysis [16,25].

4. Results and discussion

4.1. *Effects of particle thermal relaxation time*

The flame propagation speed and flame temperature as functions of the flame radius with various particle thermal relaxation time (i.e. quantified by the parameter K) are shown in Figure 1(a and b), respectively. Here the ignition energy Q is set to be zero, particle heat capacity $C = 1$, and the Lewis number $Le = 1$. It can be seen from Figure 1(a) that, in purely gaseous case, the flame propagation speed gradually increases with the flame radius and approaches a constant value when the flame radius is large, which is close to the speed of freely propagating planar flames (in the limit of $R \to +\infty$). This tendency is consistent with the findings from the previous theoretical analysis [16,17]. However, when the inert solid particles are present, the flame propagation speed is decreased, and the higher the value of K, the smaller the flame propagating speed U. This can be justified by the fact that larger K means the shorter thermal response time, and therefore faster heat exchange rate between the gas phase and particle phase, which weakens the gas phase reaction and reduces flame propagation speed.

Besides, the change of flame propagation speed with K is not monotonic, as shown in Figure 1(a). When K is small (say 0.01) or large (10), the reduction of propagation speed is relatively smaller than that corresponding to intermediate K. When K is further increased to 100, the results are nearly the same as those for $K = 10$. This implies that when the particle relaxation time is very short (large K) and very long (small K), variation of this time scale only leads to small change of flame propagation speed. Figure 1(b) shows that the flame temperatures as a function of flame radius for different K. The temperature of a purely gaseous case is always unity. However, for the particle-laden cases, the flame temperature is decreased with increased particle K (i.e. decreased particle thermal relaxation time).

4.2. *Effects of particle heat capacity*

The flame propagation speed and flame temperature as functions of the flame radius with various values of particle heat capacity (i.e. the parameter C) are shown in Figure 2. Here $Q = 0$, $K = 0.1$, and $Le = 1$ are assumed. When C is relatively small (e.g. $C = 1$ in Figure 2), the flame propagation speed continuously increases as the flame propagates outwardly and approaches the planar flame speed ($U = 1$). This is similar to the results of purely gaseous flames, as indicated in Figure 1(a). However, when $C = 3$, the flame propagation speed exhibits a non-monotonic behaviour. Specifically, it first increases, then decreases and finally is close to a constant small value (about 0.18) at large radii. This is also observed when $C = 5$ in Figure 2(a). It is noted that, according to Equation (20), the parameter C represents the ratio of the heat capacity of the particles to the heat capacity of the gas mixture. The larger the value of C, the more heat the solid particles can store, and hence the more heat loss from the gas phase. Consequently, the flame propagation speed and flame temperature decrease (see Figure 2(b)). The non-monotonic behaviours about the flame propagation speed when the particle heat capacity C is large will be discussed in Section 4.3.

Figure 3 shows the flame propagation speed as a function of the flame radius with $K = 0.025$. New patterns and bifurcations of U–R solution curves appear in this condition. When $C = 4$, the spherical flame can successfully evolve into a planar flame. Here it is still monotonic even if $C = 4$, which has already led to a non-monotonic behaviour with $K = 0.1$ as indicated in Figure 2(a). This is due to the smaller K value here, indicating

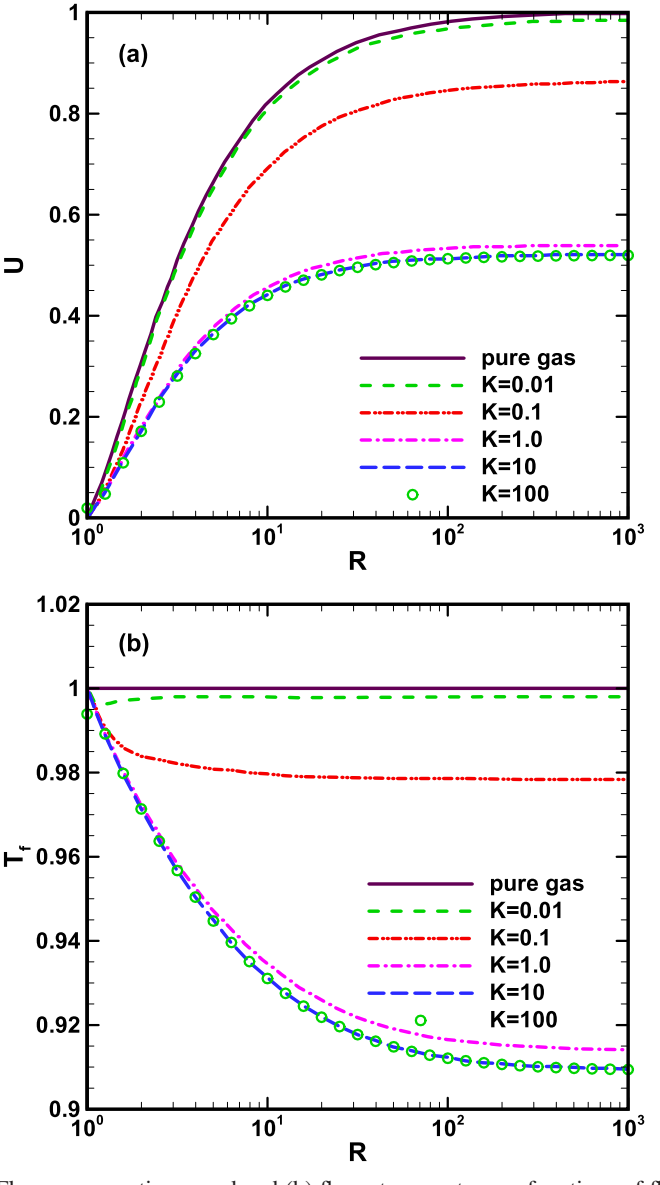

Figure 1. (a) Flame propagation speed and (b) flame temperature as functions of flame radius for $Q = 0$, $C = 1$, $Le = 1$, and different values of K.

the longer particle thermal relaxation time. Accordingly, the induced heat transfer rate is smaller, which dominates the effects from increased C (enhance the particle heat capacity and therefore weaken the spherical flame). For $C = 6.3$, two separate flame branches can be seen: the upper branch is stable, whereas the lower one has both stable and unstable solutions. When C is between 6.5 and 6.9, only one curve exists with upper stable strong flame, middle unstable flame and lower stable weak flame. Therefore, for $6.3 < \mathrm{C} < 6.9$ the flame bifurcates and multiplicity of the flame propagation speed U occurs, which was also found by Ju et al. in the theoretical analysis of particle-laden premixed planar flames

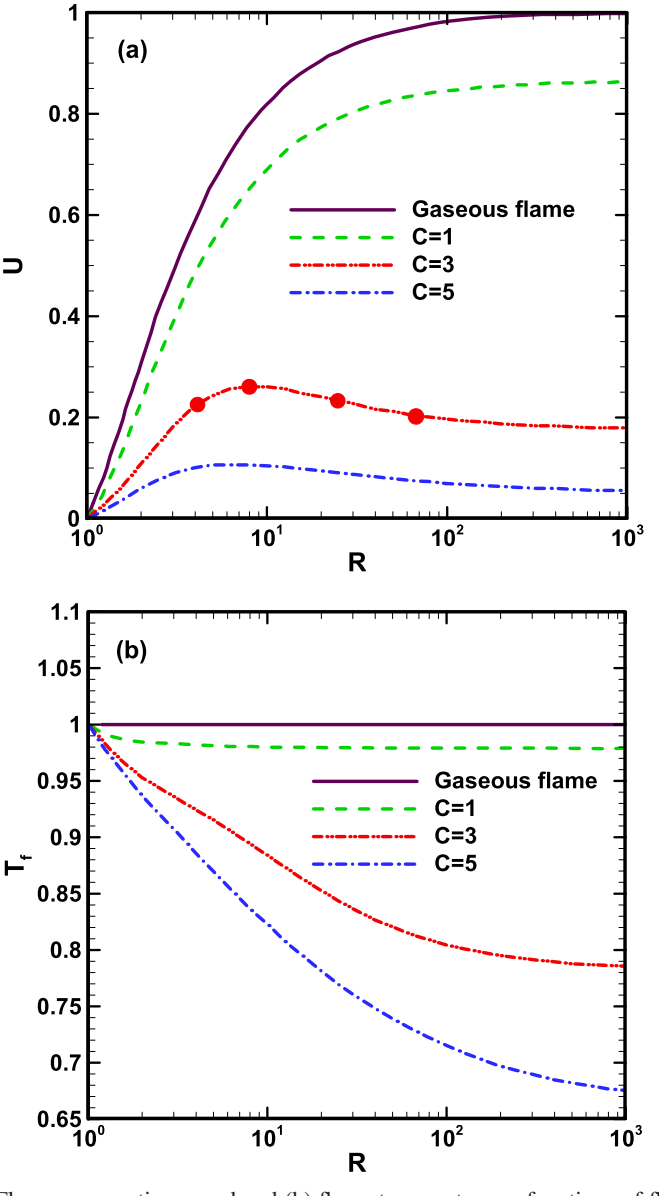

Figure 2. (a) Flame propagation speed and (b) flame temperature as functions of flame radius for $K = 0.1$, $Le = 1$, $Q = 0$, and different values of C. The solid circles in (a) indicate the flame radii, used for flame structure analysis in Figure 4.

[7]. It is noticeable from Figure 3 that extinction of a propagating flame would occur when $6.5 \leq C \leq 6.9$. Take the curve of $C = 6.5$ as an example, the flame propagation speed gradually increases with increased radius, and then reaches the maximum when $R \approx 100$, which corresponds to a critical state. As the flame propagates further, it jumps from the upper stable strong branch to the lower stable weak branch. The flame propagation speed along the lower branch is much lower than that of the upper flame branch. However, when

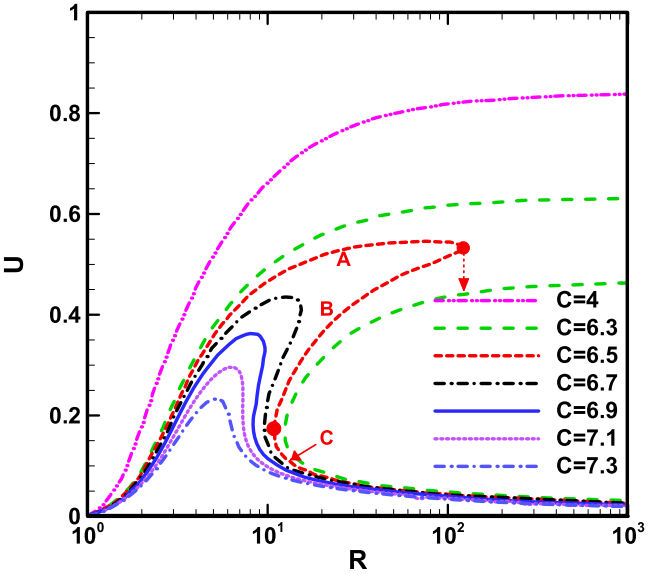

Figure 3. Flame propagation speed as a function of flame radius for $K = 0.025$, $Le = 1$, $Q = 0$, and different values of C. Circles indicates the turning points for flame bifurcations. A: upper stable flame; B: unstable flame; C: lower stable flame.

C is further increased (e.g. $C \geq 7.1$ in Figure 3), the above foregoing flame bifurcation and multiplicity cannot be seen; instead, non-monotonicity of flame propagating speed U appears, similar to the results of $C = 3$ in Figure 2(a).

4.3. *Non-monotonicity and bifurcation of particle-laden spherical flames*

The results in Section 4.2 show that in the case of $K = 0.1$ and $C = 3$ (in Figure 2), the non-monotonic behaviour of the propagation speed is observed for travelling particle-laden spherical flames. Also, under the condition of $K = 0.025$ and $6.5 \leq C \leq 6.9$ (in Figure 3) discussed in Section 4.2, flame bifurcation occurs with three various flame regimes and sudden shift from the strong to weak flames is observed. In this Sub-section, these two phenomena are investigated through analysing the corresponding temperature distributions.

Figure 4 shows the spatial distributions of gas and particle temperatures at four selected flame radii ($R = 4$, 8, 25 and 63) with the non-monotonic behaviours of U, which have been marked by solid circles in Figure 2(a). Note that the first two radii correspond to the solution curves with increasing U, while the latter two are from the solutions with declining U. It can be seen that as the spherical flame expands outwardly, the temperature of the particle in the post-flame region increases due to the heating from the hot burnt gas, while the temperatures of the flame front and the gas phase decrease. Due to the intermediate particle thermal response time ($K = 0.1$ in Figure 2(a)), the particles cannot quickly reach the thermal equilibrium with the surrounding gas. In the meantime, for spherical flames with small radii, there are limited particles inside, so the heat exchange is comparatively small. Therefore, at the early stage, the flame propagation speed can continuously increase. Nevertheless, as the flame expands further outwardly, the number of particles within the spherical flame is increased. When the energy from the chemical reaction cannot afford

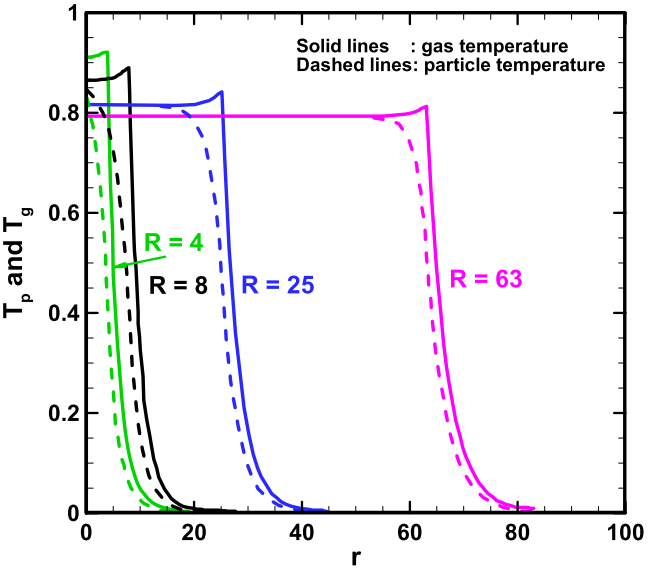

Figure 4. Distributions of gas and particle temperatures at four flame radii $R = 4$, 8, 25 and 63 (indicated in Figure 2(a) with solid circles). Here $K = 0.1$ and $C = 3$.

the excessive heat loss of the gas phase, the flame speed decreases towards a low value. However, no extinction is observed here (see Figure 2(a)), and the spherical flame can still sustain itself towards planar flame limit with low speed. This indicates that the energy from the chemical reactions and the heat loss due to the exchange between two phases can reach a new balance characterised by relatively low flame propagating speed as demonstrated in Figure 2.

Along the U-R curve of $K = 0.025$ and $C = 6.7$ in Figure 3, we selected five radii to plot their temperature distributions in Figure 5. For $R = 6$, it lies at the upper stable flame branch, while for $R = 20$ and 32, they correspond to the lower weak stable flame branch. At $R = 15$, two points are selected for discussion here, one at the turning point, whilst the other at the lower flame branch. It is found from Figure 5 that the temperature distributions along the upper and lower flame branches have a pronounced difference. Specifically, the particle temperatures along the upper flame branch are significantly lower than the gas temperature. Furthermore, this inter-phase temperature difference always exists with an increased flame radius, e.g. from $R = 6$–15. The particle temperatures from the lower flame branch considerably increase, and also the temperature difference between the two phases decreases. For $R = 15$, when the flame is at the upper branch, its temperature is not significantly reduced than that at $R = 6$. In addition, the gas temperature is consistently higher than the particle temperature. When it jumps to the lower branch ($R > 15$), the gas temperature is significantly reduced, whereas the particle temperature is increased.

The evolutions of the temperatures of both phases along the upper stable branch can be justified by the smaller value of K (i.e. 0.025) in this case, indicating the relatively longer particle thermal relaxation time. This results in slower heat transfer between the two phases, so the particle temperature is smaller and the temperature difference between two phases for the shown radius range is more pronounced. When the spherical flame propagates outwardly, its radius increases and more particles travel through the flame front

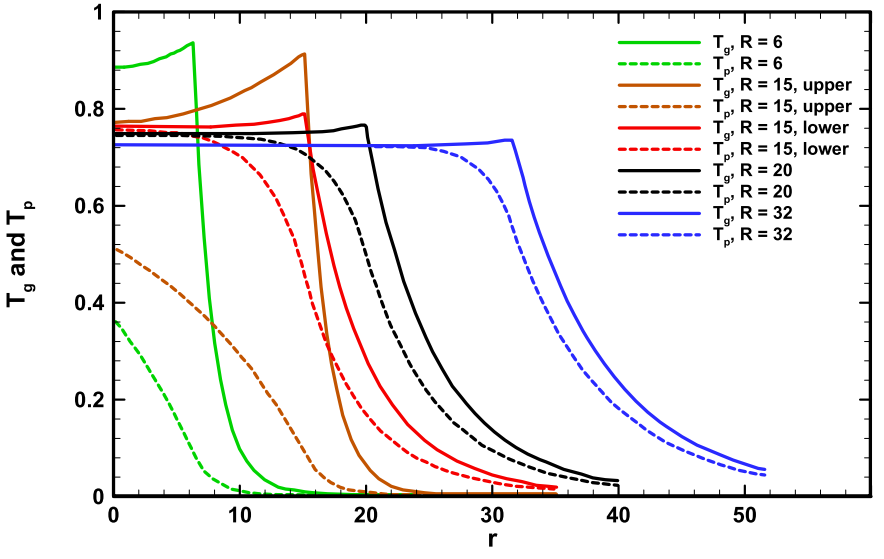

Figure 5. Distributions of gas and particle temperature at various flame radii $R = 6$, 15, 20 and 32. For $R = 15$, there are two selected radii, at upper and lower branches, respectively. Here $K = 0.025$ and $C = 6.7$.

and are dispersed in the burned zone. When a critical amount of solid particles is involved, the heat transfer between gas and particle may lead to excessively energy loss in the gas phase. In this scenario, the energy released from the chemical reaction cannot support the self-sustained propagation of the spherical flame. A sudden decrease in flame propagation speed and temperature would help to build a new equilibrium between two phases along the lower weak flame branch, see the temperature distributions at three radii ($R = 15$, 20 and 32) along the weak flame branch.

In summary, the flame bifurcation phenomenon, which results in the jump from strong flame to weak flame, occurs under the combined conditions of a small K value and a large C value. A small K represents a large particle thermal response time, whilst a large C indicates a high particle heat capacity and therefore large total heat loss for the gas phase. This combination can make the heat exchange effect comparatively small at the initial stage, so the flame propagation speed continuously increases. When the spherical flame propagates at a large radius, the gas heat loss becomes large due to accumulated solid particles, and the flame cannot sustain itself, and then sudden transition occurs from strong to weak flames.

4.4. *Effects of Lewis number*

The influence of the Lewis number on the flame propagation is investigated here with $K = 0.1$, $C = 1$ and $Q = 0$. Figure 6(a) shows the flame propagation speed as a function of radius for $Le = 0.5$, 1 and 2. For comparisons, the gaseous flames with the same Le numbers are also shown. It is well known that for gaseous flames the influences of the stretch rate on the flame propagation speed are highly dependent on the Lewis number Le [16,17,32]. As presented in Figure 6(a), the particle-laden spherical flame has similar propagation behaviours to those of gaseous flames with the same Lewis numbers. The inclusion of inert solid particles does not qualitatively change the shapes of U-R curves for the same

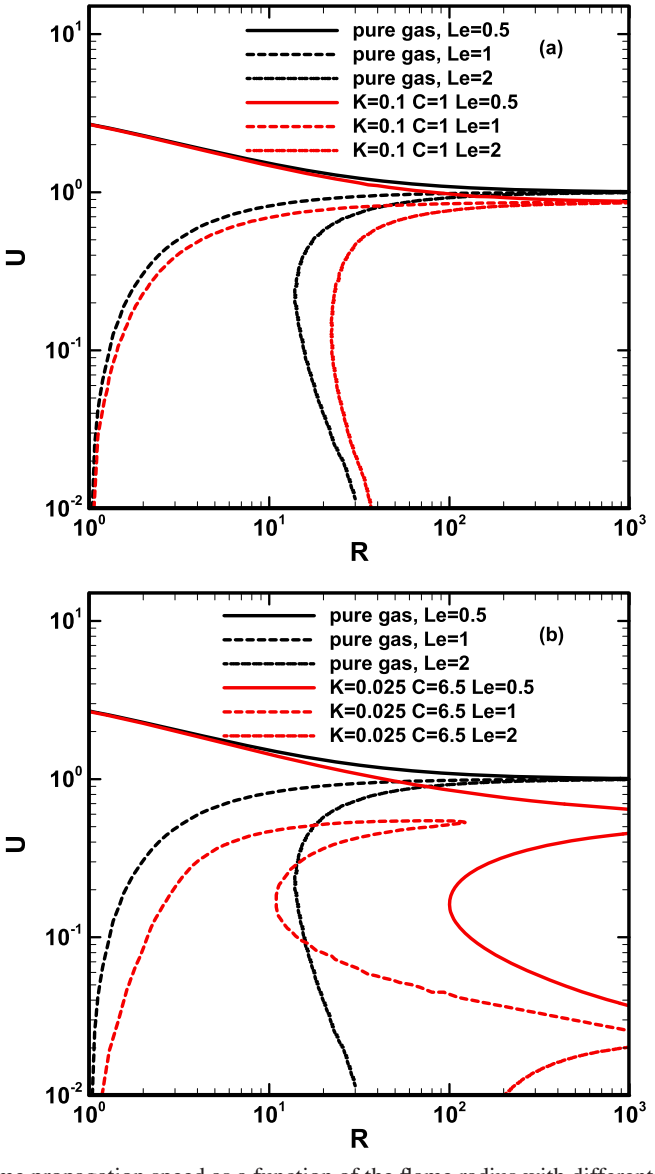

Figure 6. Flame propagation speed as a function of the flame radius with different Lewis numbers ($Le = 0.5$, 1 and 2). (a) $K = 0.1$ and $C = 1$; (b) $K = 0.025$ and $C = 6.5$. Particle-free cases with $Le = 0.5$, 1 and 2 are also shown for comparisons.

Lewis numbers. However, generally, the flame propagation speed is reduced in particle-laden cases compared to that in gaseous cases. This is caused by the heat loss effects from the solid particles. Exceptions are the propagation speed of spherical flames with small radius and Lewis number (say $Le = 0.5$ in Figure 6(a)), where negligible reduction can be observed for $R < 5$. In this case, the enhancement of the flame propagation speed due to the positive stretch and smaller Lewis number may dominate the particle-induced heat loss, and therefore the influences from the latter are relatively small.

Figure 6(b) shows the flame propagation speed from the case of $K = 0.025$, $C = 6.5$ and $Q = 0$. The Lewis number considerably affects the U-R curves from the particle-laden and particle-free cases. For $Le = 0.5$, there are three flame speeds when R is large (say $R = 10^3$) and they are from upper stable branch, middle unstable branch and lower stable branch, respectively. The latter two are not present in the gaseous flame with $Le = 0.5$. For $Le = 1$, the jump from the upper branch to lower stable branch occurs, which has been discussed in Figure 3, and there is only one flame speed for the large radius (e.g. $R > 200$). When $Le = 2$, the flame propagation speed is very low, and only one branch appears. Therefore, the dependence of flame propagation speed on the flame radius can be affected by the Lewis number qualitatively and/or quantitatively due to the heat loss from the solid particles.

4.5. *Effects of central ignition energy*

In this Sub-section, the effects of central ignition energy Q on propagation of the spherical flame with inert solid particles are investigated. Figure 7(a and b) show the flame propagation speeds as functions of flame radius for gaseous flame and particle-laden flame, respectively. Here, $Le = 1$, $K = 0.1$ and $C = 1$ are assumed. Overall, in this case, the presence of the inert particles does not change the pattern of the U–R curves. It can be seen from Figure 7 that, besides the right travelling flame branch, the left flame kernel branch at small radii arises due to the deposition of ignition energy Q at the spherical centre. When Q is small, along the flame kernel branch, the flame propagation speed rapidly decreases to zero and the flame is extinguished at the flame ball radius (corresponding to $U = 0$). This corresponds to ignition failure of the spherical flame. The critical radius of the right branch is reduced compared to that with $Q = 0$. As the ignition energy Q is further increased, the two branches become close, finally merge and form a curve. This corresponds to the critical successful ignition of the spherical flame. In this situation, the spherical flame is initiated from the flame kernel, then propagates outwardly and finally approaches the planar flame. For both cases, the MIE is close, i.e. $Q_{min} = 0.065$ for the pure gas flame while $Q_{min} = 0.068$ for the particle-laden flame. However, as shown in Figure 7(a and b), the flame propagation speed of travelling branch in the particle-laden case is lower than that in the gaseous case, caused by the heat loss from the inert solid particles.

The results of Lewis number $Le = 2$ are shown in Figure 8. Similar to Figure 7, Figure 8(a and b) correspond to gaseous and particle-laden cases, respectively. Here the travelling flame branch is C-shaped, different from the results in Figure 7. It is worth noting that when Lewis number Le is large (e.g. here $Le = 2$), increasing the ignition energy has a limited effect on the right branch. Conversely, with increased Q, the left branch continuously moves to the right branch and finally merges into one curve, which corresponds to successful ignition. By comparing the two cases in Figure 8(a and b), it is also found that the presence of inert particles does not qualitatively change the flame bifurcation, but leads to an increase of MIE (from 1.97 in the purely gaseous case to 2.4 in particle-laden case).

Figure 9 demonstrates the MIE Q_{min} as a function of Lewis number Le. Here Q_{min} is calculated through the calculations of U–R curves using the trial-and-error method, with relative error less than 5%. Both gaseous and particle-laden flames are considered. For the latter, $K = 0.1$ and $C = 1$ are assumed. As in Figure 9, for both situations, Q_{min} increases with Lewis number. This tendency is also observed in ignition of particle-free gaseous

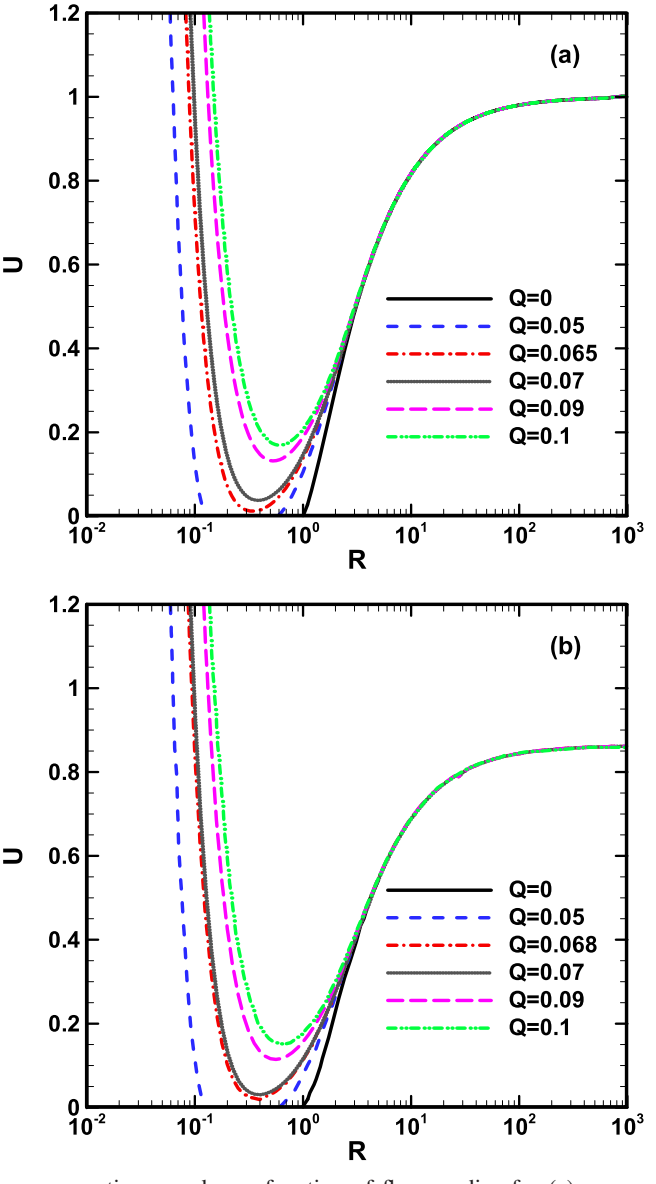

Figure 7. Flame propagation speed as a function of flame radius for (a) gaseous flame and (b) particle-laden flame. For the particle-laden case, $Le = 1$, $K = 0.1$, and $C = 1$ are assumed.

spherical flames through our recent theoretical analysis [16,17]. When Lewis number is less than 1.7 as shown in Figure 9, MIE corresponding to both cases is close to each other. Nevertheless, when it is greater than 1.7, the MIE difference between them starts to increase with Lewis number. For the spherical premixed flames, when Lewis number increases, the extent to which they are weakened by the combined effects of Lewis number and the positively stretched rate becomes large. In this situation, the influences of the particles dispersed in the pre-mixture on MIE are pronounced.

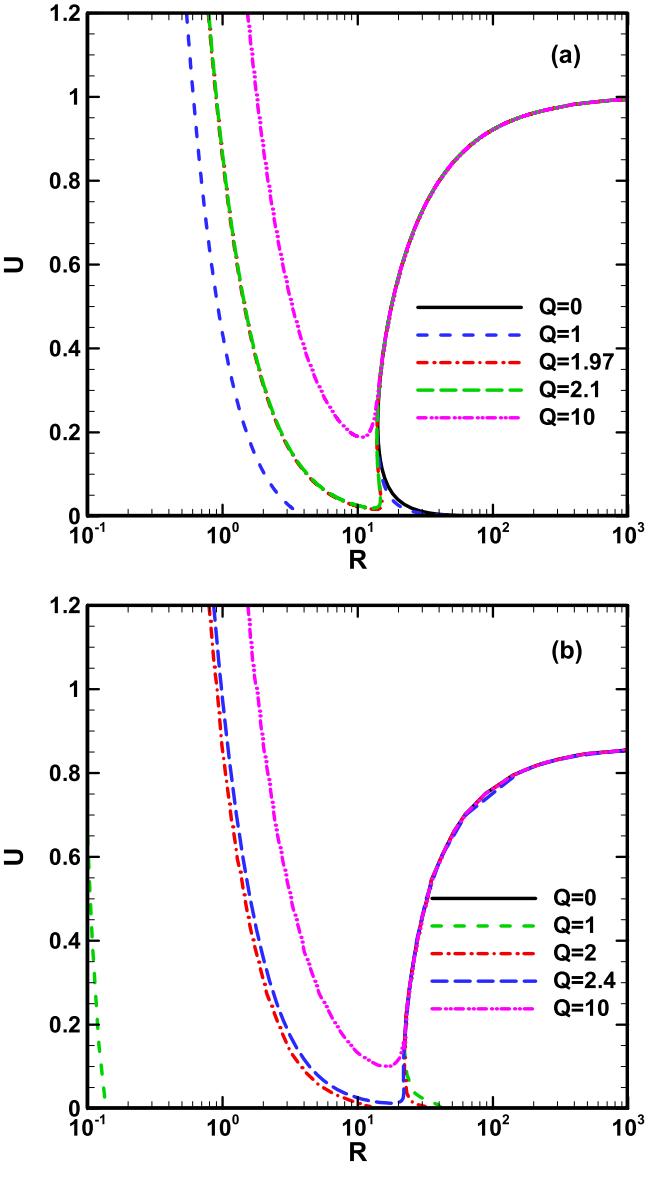

Figure 8. Flame propagation speed as a function of flame radius for (a) gaseous flame and (b) particle-laden flame. For the particle-laden case, $Le = 2$, $K = 0.1$, and $C = 1$ are assumed.

5. Numerical validation

Assumptions, such as quasi-steady-state and large activation energy, are introduced to perform the above theoretical analysis. To examine the validity of the findings from the above analysis, transient simulations of particle-laden spherical premixed flames are performed with a time-accurate and space-adaptive numerical solver, A-SURF [17,32–34]. The accuracy of A-SURF on propagating gaseous spherical flames has been validated extensively in previous studies [17,32–34]. The Eulerian solver for the particle phase is

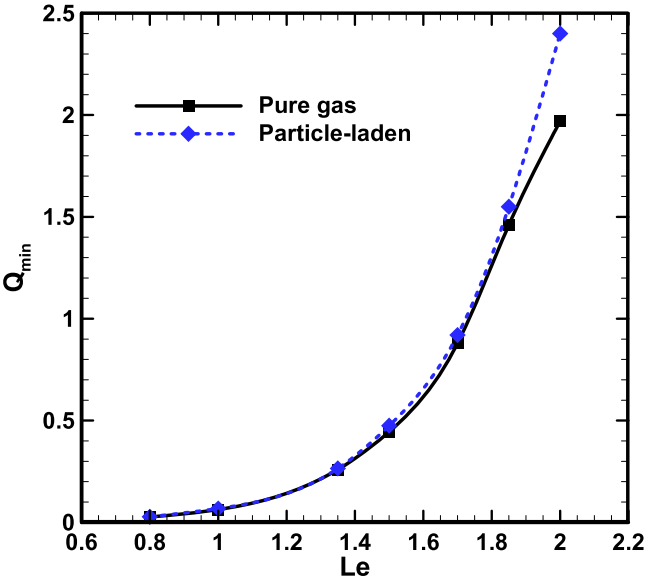

Figure 9. Minimum ignition energy as a function of Lewis number for gaseous and particle-laden flames. For the particle-laden case, $K = 0.1$ and $C = 1$ are assumed.

implemented in A-SURF, and two-way coupling is performed between the gas phase and solid particle phase, in terms of mass, momentum, and energy exchanges. The governing equations and sub-models in the Eulerian solver for the solid particle phase are detailed in the supplemental document.

In our simulations, the computational domain is set to be $0 \leq r \leq 100$cm and the minimum mesh size is $8\,\mu$ m. The boundary conditions at the left ($r = 0$) and right ($r = 100$ cm) are set to be zero gradient. The gas mixture is initially quiescent with 300 K and 1 atm. The initial particle temperature is 298 K and the number density is 8000 1/cm^3. The mixture is composed of H_2/O_2/Ar/He. Ar and He account for 70% (by vol.) in total, and the equivalence ratio is fixed to be 2. A detailed chemical mechanism developed by Li et al. [35] is used in the simulations.

To mimic spark ignition, an energy source is placed at the left boundary (i.e. at spherical centre $r = 0$) to provide an energy deposition lasted for a given ignition time τ_{ig} as [36]

$$q_{ig}(r,t) = \begin{cases} \dfrac{E_{ig}}{\pi^{1.5} r_{ig}^3 \tau_{ig}} \exp\left[-\left(\dfrac{r}{r_{ig}}\right)^2\right] & \text{if } t < \tau_{ig}, \\ 0 & \text{if } t \geq \tau_{ig}, \end{cases} \tag{47}$$

where E_{ig} is the total ignition energy and r_{ig} is the ignition kernel radius. In this study, $\tau_{ig} = 200\,\mu$ s and $r_{ig} = 200\,\mu$ m are assumed, following Chen et al. [37]. Unless otherwise stated, the total ignition energy E_{ig} used is sufficiently large, i.e. 0.8 mJ, to achieve successful ignition.

Here the effects of particle thermal response time, particle heat capacity and mixture Lewis number on initiation and propagation of spherical flames will be investigated. The Lewis number can be adjusted through changing the helium volumetric fraction in the mixture of H_2/O_2/Ar/He, since the thermal diffusivity of the pre-mixture increases due

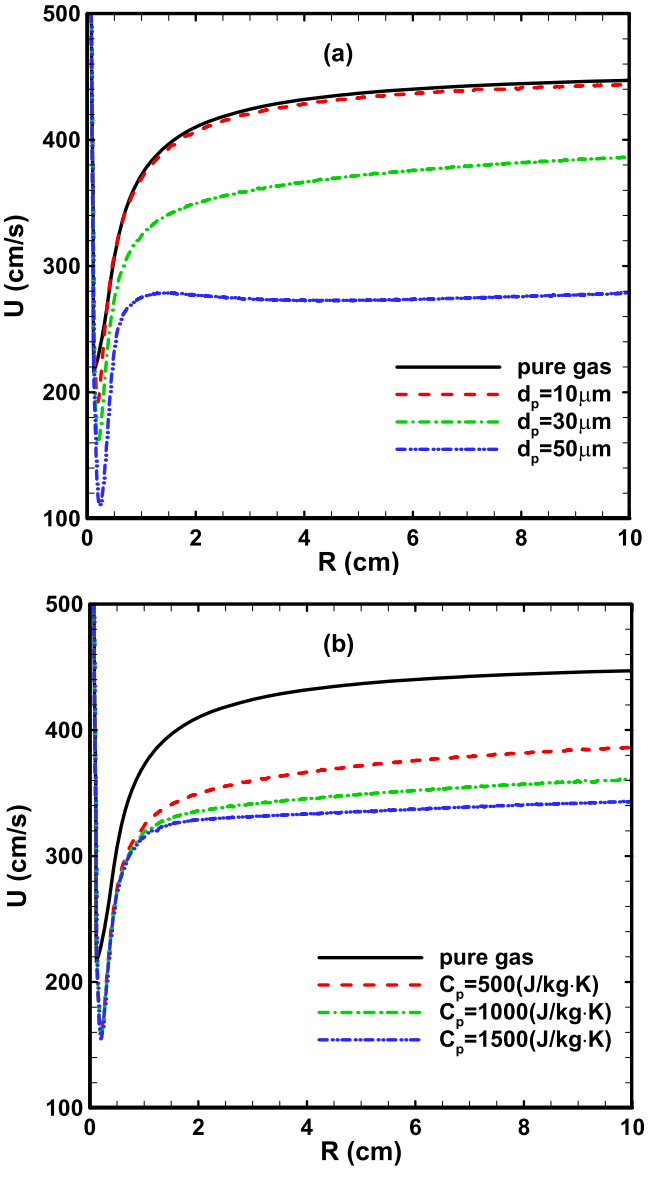

Figure 10. Flame propagation speed as a function of flame radius for different (a) particle diameters (with fixed $\tilde{C}_{p,p} = 500\,\mathrm{J/kg/K}$) and (b) particle heat capacity (with fixed $\tilde{d}_p = 30\,\mu\mathrm{m}$).

to the large helium fraction [37]. For particle heat capacity, three values (500, 1000 and 1500 J/kg/K) are selected to examine its influence on spherical flame propagation. The particle thermal response time can be estimated as [1]

$$\tau_T = \frac{\tilde{\rho}_p \tilde{C}_{p,p} \tilde{d}_p^2}{12\tilde{\lambda}}, \tag{48}$$

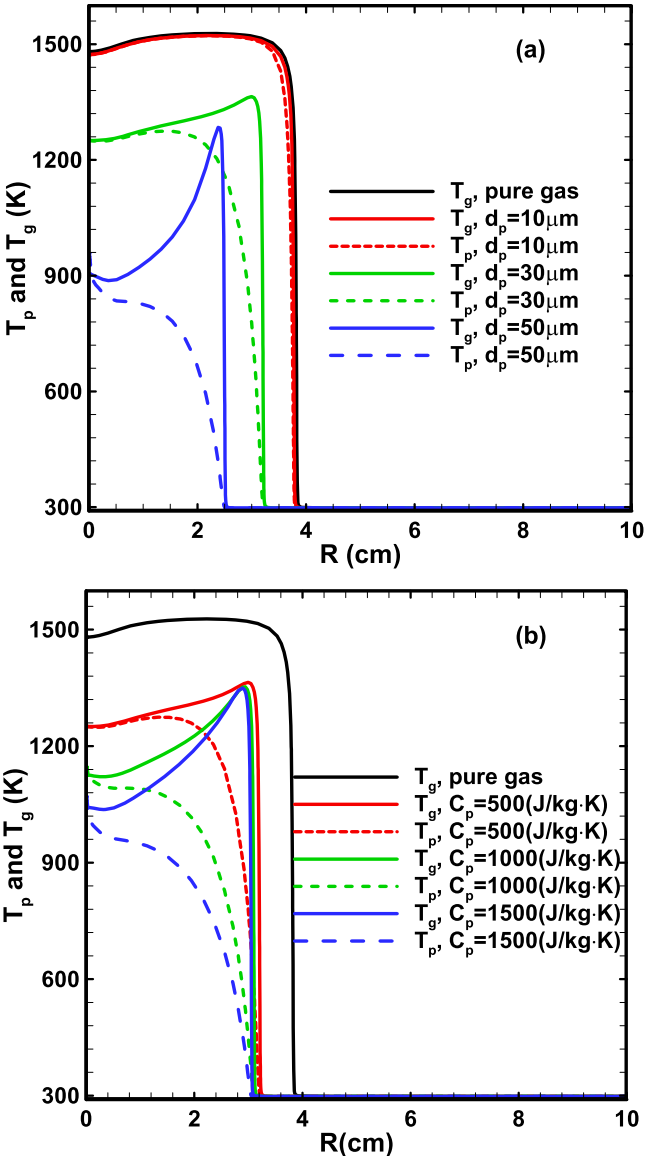

Figure 11. Distributions of gas and particle temperatures with different (a) particle diameters (with fixed $\tilde{C}_{p,p} = 500$ J/kg/K) and (b) heat capacities (with fixed $\tilde{d}_p = 30\,\mu$m).

which shows that the thermal response time τ_T is a function of the particle heat capacity and diameter. Therefore, we will also study the particle diameter effects on the initiation and propagation of spherical flames. In general, larger particles have a longer thermal response time, indicating that it takes a longer time to establish the thermal equilibrium between the gas and particle phases.

Figure 10 shows the flame propagation speed as a function of flame radius with various values of particle diameter and heat capacity. The solid particles show a significant influence on the propagation of spherical flames, which can be clearly seen in Figure 10

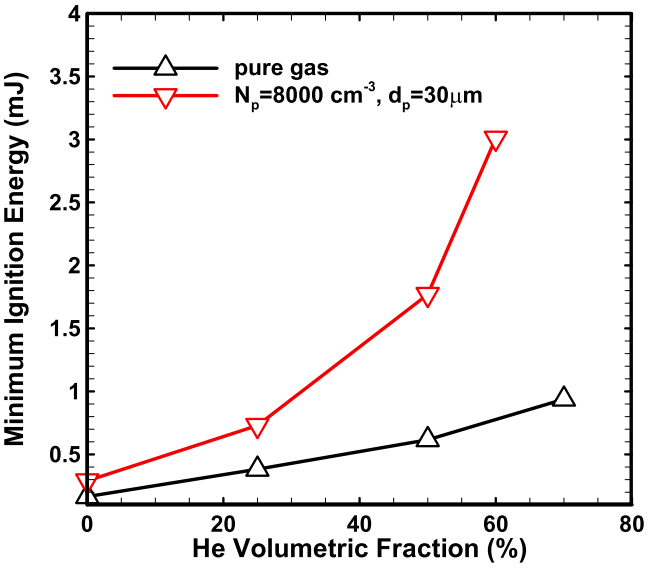

Figure 12. Minimum ignition energy as a function of helium volumetric fraction in the initial mixture.

through comparisons with the purely gaseous flames. Specifically, the increase in the particle diameter and heat capacity could lead to a decrease in the flame propagation speed. When the particle diameter is small (say 10 μ m in Figure 10), the reduction of the flame propagation speed is comparatively small. When the diameter is further increased, the propagation speed is substantially reduced, e.g. approximately 15% for 30 μ m and 38% for 50 μ m compared to that of purely gaseous flame. For the selected particle heat capacity in Figure 10(b), the propagation speed is decreased by about 15%, 20% and 23%, respectively, compared to the gaseous flame situation. Since particle diameter and heat capacity are directly related to the thermal response time as given in Equation (48), the observations made here are qualitatively consistent with those from the theoretical analysis shown in Figure 1 and 2.

Figure 11 shows the spatial distributions of gas and particle temperatures in propagating spherical flame laden with solid particles of different diameters and heat capacities. Here the estimated particle thermal relaxation time K from Equation (19) is between 0.013 and 0.95. All the results in Figure 11 correspond to $t = 0.01$ s ($t = 0$ s corresponds to the flame initiation time). For small particles with diameter of 10 μ m, the temperature difference between gas and solid particles in the burned zone is negligible, which implies that the thermal response time is short and the equilibrium has been established for the shown radius range. When the diameter is increased, both gas and particle temperatures are considerably reduced. The gas temperature gradients in the burned zones become steeper with increased diameter, which would further cool down the flame through heat conduction. The distance behind the flame front to reach the thermal equilibrium is longer with a larger particle diameter. Since all the results shown in Figure 11(a) are from $t = 0.01$ s, one can also observe that the increased particle diameter slows down the propagating spherical flames, which is in line with what is shown in Figure 10(a). In addition, one can see from Figure 11(b) that increased particle heat capacity leads to lower gas temperature in the burned zone and therefore larger gas temperature gradient, although the temperature at the

flame front is negligibly affected. Compared to the particle diameter, heat capacity shows a comparatively small influence on flame propagation speed, which is also presented in Figure 10.

Plotted in Figure 12 is the MIE as a function of helium volumetric fraction in the particle-laden mixture. Here the particle diameter is assumed to be 30 μm. For comparisons, the MIEs from gaseous flames are also plotted in Figure 12. The MIE is determined through the method of trial-and-error with relative error less than 5%. As the helium volumetric fraction is increased (indicating the increased Lewis number here), the MIE monotonically increases for the shown range of helium fractions. This tendency is also found for gaseous flame case, as shown in Figure 12. Nevertheless, the MIEs of the particle-laden mixture are about 40–50% higher than those of gaseous flames. When the volumetric fraction of helium is larger than 60%, the particle-laden mixture is very difficult to be ignited, quantified by the considerably increased MIE ($>$ 10 mJ). Their MIEs are not indicated in Figure 12. As such, the dependence of MIE on the Lewis number indicated from the present numerical simulations is qualitatively in accordance with theoretical results in Figure 9.

6. Conclusions

Initiation and propagation of spherical flames laden with chemically inert solid particles are investigated theoretically. Within the framework of large activation energy and quasi-steady assumptions, a correlation describing spherical flame propagation speed as a function of flame radius is derived. With this correlation, the influences of gas and particle properties (e.g. Lewis number, particle thermal response time and heat capacity) on the initiation and propagation of spherical flames can be assessed.

The results indicate that particle thermal response time could affect the heat transfer between gas and particle phases, and a higher thermal response time leads to a faster rate to reach the thermal equilibrium. In addition, particle heat capacity quantifies the heat storage capacity, and more heat is transferred from the gas to the particle with a higher particle heat capacity. Therefore, the flame propagation speed and temperature are decreased with increased particle thermal response time and heat capacity. A non-monotonic variation of the flame propagation speed is observed for large particle heat capacity. This can be justified by the balance between heat release from chemical reactions and heat loss due to the gradually increased solid particles in the burned zone of an outwardly propagating spherical flames. In addition, multiplicity and bifurcation of flame propagation speed are present under some critical conditions (e.g. large particle heat capacity and thermal relaxation time). This is caused by the combined effects of large particle heat capacity and thermal relaxation time, which results in the excessive heat loss from the solid particles and therefore flame extinction occurs. The Lewis number strongly affects the flame propagation speed, particularly for small thermal response time and high particle heat capacity. Besides, the minimum ignition energy of the particle-laden flames is shown to increase with the Lewis number. With the increase of Lewis number, the difference of minimum ignition energy between gaseous and particle-laden spherical flames increases.

It is noted that the theoretical analysis is constrained by constant-density, quasi-steady and large activation energy assumptions. To confirm the validity of theoretical prediction, one-dimensional transient numerical simulations of particle-laden spherical flames with detailed chemistry and Eulerian particle model have been conducted to examine the effects

of Lewis number and solid particle properties on initiation and propagation of spherical flames. The numerical results agree qualitatively with those from theoretical analysis.

Disclosure statement

No potential conflict of interest was reported by the author(s).

Funding

QL is sponsored by the National University of Singapore (NUS) Research Scholarship. HZ is supported by the start-up grant (R-265-000-604-133) from NUS. ZC is supported by the National Natural Science Foundation of China (Nos. 51861135309 and 91741126).

Supplemental data

Supplemental data for this article can be accessed at https://doi.org/10.1080/13647830.2020.1725135.

ORCID

Huangwei Zhang http://orcid.org/0000-0002-5215-5712
Zheng Chen http://orcid.org/0000-0001-7341-6099

References

[1] C. Crowe, J. Schwarzkopf, M. Sommerfeld and Y. Tsuji, *Multiphase Flows with Droplets and Particles*, 2nd ed., CRC Press, Boca Raton, FL, 2011.
[2] G. Joulin, *Asymptotic analysis of non-adiabatic flames: heat losses towards small inert particles*. Proc. Combust. Inst. 18 (1981), pp. 1395–1404.
[3] T. Mitani, *A flame inhibition theory by inert dust and spray*. Combust. Flame 43 (1981), pp. 243–253.
[4] T. Mitani and T. Nhoka, *Comparison of experiments and theory on heterogeneous flame suppressants*. Proc. Combust. Inst. 19 (1982), pp. 869–875.
[5] R. Blouquin, P. Cambray and G. Joulin, *Radiation-affected dynamics of enclosed spherical flames propagating in particle-laden premixtures*. Combust. Sci. Technol. 128 (1997), pp. 231–255.
[6] R. Blouquin and G. Joulin, *Radiation-affected hydrodynamic instability of particle-laden flames*. Combust. Sci. Technol. 110–111 (1995), pp. 341–359.
[7] Y. Ju and C.K. Law, *Dynamics and extinction of non-adiabatic particle-laden premixed flames*. Proc. Combust. Inst. 28 (2000), pp. 2913–2920.
[8] G.M. Makhviladze, O.I. Melikhov, J.P. Roberts and G.I. Sivashinsky, *Effects of momentum nonequilibrium on flame propagation and extinction in the presence of inert particles*. Combust. Flame 106 (1996), pp. 333–344.
[9] M. Frankel and G. Sivashinsky, *On quenching of curved flames*. Combust. Sci. Technol. 40 (1984), pp. 257–268.
[10] S.H. Chung and C.K. Law, *An integral analysis of the structure and propagation of stretched premixed flames*. Combust. Flame 72 (1988), pp. 325–336.
[11] P. Ronney and G. Sivashinsky, *A theoretical study of propagation and extinction of nonsteady spherical flame fronts*. SIAM J. Appl. Math. 49 (1989), pp. 1029–1046.
[12] J.K. Bechtold and M. Matalon, *Hydrodynamic and diffusion effects on the stability of spherically expanding flames*. Combust. Flame 67 (1987), pp. 77–90.
[13] M. Matalon, C. Cui and J.K. Bechtold, *Hydrodynamic theory of premixed flames: effects of stoichiometry, variable transport coefficients and arbitrary reaction orders*. J. Fluid Mech. 487 (2003), pp. 179–210.
[14] J. Bechtold, C. Cui and M. Matalon, *The role of radiative losses in self-extinguishing and self-wrinkling flames*. Proc. Combust. Inst. 30 (2005), pp. 177–184.

[15] L. He, *Critical conditions for spherical flame initiation in mixtures with high Lewis numbers*. Combust. Theory Model. 4 (2000), pp. 159–172.
[16] Z. Chen and Y. Ju, *Theoretical analysis of the evolution from ignition kernel to flame ball and planar flame*. Combust. Theory Model. 11 (2007), pp. 427–453.
[17] H. Zhang and Z. Chen, *Spherical flame initiation and propagation with thermally sensitive intermediate kinetics*. Combust Flame 158 (2011), pp. 1520–1531.
[18] H. Li, H. Zhang and Z. Chen, *Effects of endothermic chain-branching reaction on spherical flame initiation and propagation*. Combust. Theory Model 23(2019) (2018), pp. 496–514.
[19] H. Zhang, P. Guo and Z. Chen, *Critical condition for the ignition of reactant mixture by radical deposition*. Proc. Combust. Inst. 34 (2013), pp. 3267–3275.
[20] J.B. Greenberg, *Finite-rate evaporation and droplet drag effects in spherical flame front propagation through a liquid fuel mist*. Combust. Flame 148 (2007), pp. 187–197.
[21] W. Han and Z. Chen, *Effects of finite-rate droplet evaporation on the ignition and propagation of premixed spherical spray flame*. Combust. Flame 162 (2015), pp. 2128–2139.
[22] Y. Zhuang and H. Zhang, *Effects of water droplet evaporation on initiation, propagation and extinction of premixed spherical flames*. Int. J. Multiphase Flow 117 (2019), pp. 114–129.
[23] L. Qiao, *Transient flame propagation process and flame-speed oscillation phenomenon in a carbon dust cloud*. Combust. Flame 159 (2012), pp. 673–685.
[24] H. Zhang, P. Guo and Z. Chen, *Outwardly propagating spherical flames with thermally sensitive intermediate kinetics and radiative loss*. Combust. Sci. Technol. 185 (2013), pp. 226–248.
[25] Y. Wu and Z. Chen, *Asymptotic analysis of outwardly propagating spherical flames*. Acta Mech. Sin. 28 (2012), pp. 359–366.
[26] G. Joulin and P. Clavin, *Linear stability analysis of nonadiabatic flames: Diffusional-thermal model*. Combust. Flame 35 (1979), pp. 139–153.
[27] H. Zhang and Z. Chen, *Effects of heat conduction and radical quenching on premixed stagnation flame stabilised by a wall*. Combust. Theory Model. 17 (2013), pp. 682–706.
[28] H. Zhang and Z. Chen, *Bifurcation and extinction limit of stretched premixed flames with chain-branching intermediate kinetics and radiative loss*. Combust. Theory Model. 22 (2018), pp. 531–553.
[29] W.E. Ranz and J.W.R. Marshall, *Evaporation from Drops, Part I.* Chem. Eng. Prog. 48 (1952), pp. 141–146.
[30] G. Joulin, *Point-source initiation of lean spherical flames of light reactants: an asymptotic theory*. Combust. Sci. Technol. 43 (1985), pp. 99–113.
[31] A.B.O. Daalhuis, *Confluent hypergeometric functions*, in *NIST Handbook of Mathematical Functions*, F.W.J. Olver, D.W. Lozier, R.F. Boisvert, C.W. Clark, eds., Cambridge Univ., New York, 2010. pp. 321–349.
[32] Z. Chen, M.P. Burke and Y. Ju, *Effects of Lewis number and ignition energy on the determination of laminar flame speed using propagating spherical flames*. Proc. Combust. Inst. 32 (2009), pp. 1253–1260.
[33] Z. Chen, X. Qin, B. Xu, Y. Ju and F. Liu, *Studies of radiation absorption on flame speed and flammability limit of CO_2 diluted methane flames at elevated pressures*. Proc. Combust. Inst. 31 (2007), pp. 2693–2700.
[34] Z. Chen, M.P. Burke and Y. Ju, *Effects of compression and stretch on the determination of laminar flame speeds using propagating spherical flames*. Combust. Theory Model. 13 (2009), pp. 343–364.
[35] J. Li, Z. Zhao, A. Kazakov and F.L. Dryer, *An updated comprehensive kinetic model of hydrogen combustion*. Int. J. Chem. Kinet. 36 (2004), pp. 566–575.
[36] A. Frendi and M. Sibulkin, *Dependence of minimum ignition energy on ignition parameters*. Combust. Sci. Technol. 73 (1990), pp. 395–413.
[37] Z. Chen, M.P. Burke and Y. Ju, *On the critical flame radius and minimum ignition energy for spherical flame initiation*. Proc. Combust. Inst. 33 (2011), pp. 1219–1226.